Journal of Computational Physics 409 (2020) 109354

Contents lists available at ScienceDirect

Journal of Computational Physics

www.elsevier.com/locate/jcp

Numerical simulation of a coupled system of Maxwell equations and a gas dynamic model

Maohui Lyu [a], Weng Cho Chew [b], Lijun Jiang [c], Maojun Li [d], Liwei Xu [d,*]

[a] College of Mathematics and Statistics, Chongqing University, Chongqing, 401331, China
[b] School of Electrical and Computer Engineering, Purdue University, West Lafayette, IN 47907, USA
[c] Department of Electrical and Electronic Engineering, The University of Hong Kong, Hong Kong
[d] School of Mathematical Sciences, University of Electronic Science and Technology of China, Sichuan 611731, China

ARTICLE INFO

Article history:
Received 17 June 2019
Received in revised form 20 January 2020
Accepted 19 February 2020
Available online 20 February 2020

Keywords:
Discontinuous Galerkin method
Maxwell equations
Gas dynamic model
Quantum pressure
Nonlocal effect
High order harmonic generation

ABSTRACT

It is known that both linear and nonlinear optical phenomena can be produced when the plasmon in metallic nanostructures are excited by the external electromagnetic waves. In this work, a coupled system of Maxwell equations and a gas dynamic model including a quantum pressure term is employed to simulate the plasmon dynamics of free electron fluid in different metallic nanostructures using a discontinuous Galerkin method. Numerical benchmarks demonstrate that the proposed numerical method can simulate both the high order harmonic generation and the nonlocal effect from metallic nanostructures. Based on the switch-on-and-off investigation, we can conclude that the quantum pressure term in gas dynamics is responsible for the bulk plasmon resonance. In addition, for the dielectric-filled nano-cavity, a coupled effective polarization model is further adopted to investigate the optical behavior of bound electrons. Concerning the numerical setting in this work, a strengthened influence of bound electrons on the generation of high order harmonic waves has been observed.

1. Introduction

In recent years, there have been growing interests in complex optical phenomena associated with metallic nanostructures. One of them is the classical local optical response that features the macroscopic properties of materials. However, for small metallic nanoparticles and metallic clusters, the experimental studies [5] have retrieved a size-dependent surface resonance shift and a multiple bulk resonance at frequencies above the plasma frequency in the extinction cross sections (ECS). These novel phenomena, which are not observed in the classical local response, are due to the instantaneous response to the excitation in a nonlocal manner: $\mathbf{D}(\boldsymbol{x},\omega) = \epsilon_0 \int \boldsymbol{\epsilon}(\boldsymbol{x},\boldsymbol{x}',\omega)\cdot\mathbf{E}(\boldsymbol{x}',\omega)d\boldsymbol{x}'$, and thus are termed as the so-called nonlocal effect. Here, $\mathbf{D}$ is the electric displacement, ϵ_0 is the electric permittivity in vacuum, $\boldsymbol{\epsilon}$ is the relative permittivity tensor, ω is the frequency, and $\mathbf{E}$ denotes the electric field. These plasmonic responses have found their wide applications in biosensing [1], plasmonic waveguiding [3] and cancer therapy [15]. Another attractive optical phenomenon is the high order harmonic generation, in particular, the second harmonic generation (SHG). Physically, the SHG is an optical process in which an electromagnetic wave at the fundamental frequency interacts with metallic nanoparticles to generate a new

* Corresponding author.
E-mail addresses: marvin0639@gmail.com (M. Lyu), wcchew@purdue.edu (W.C. Chew), jianglj@hku.hk (L. Jiang), limj@uestc.edu.cn (M. Li), xul@uestc.edu.cn (L. Xu).

https://doi.org/10.1016/j.jcp.2020.109354
0021-9991/

wave with twice of the fundamental frequency. Experiments [12,13,19,26] have shown that the second harmonic wave can be generated from various metamaterials. The SHG is of great importance with broad applications such as in development of the laser sources [21], the optical parametric amplifiers [31], and imaging and microscopy technology [4].

There have been many numerical methods and models proposed to simulate the above optical phenomena in nanostructures. In [16], the authors generalized a finite-difference time domain (FDTD) method to simulate the SHG from metallic nanostructures by using a fully coupled fluid-Maxwell system (called the nonlinear hydrodynamic Drude (NHD) model) that was derived from the cold-plasma wave equations [32] and the Maxwell equations. In the coupled system, the charge density ρ depends on the divergence of the electric field $\mathbf{E}$, namely, $\rho = \epsilon_0 \nabla \cdot \mathbf{E}$. Since the normal electric field is discontinuous at the dielectric-metal interface, the computation of the charge density is challenging. The authors introduced a smooth transition layer between the metal and dielectric materials so that the ion density varies from its bulk value to zero smoothly, leading to an efficient computation of $\nabla \cdot \mathbf{E}$. In [14], a fully second order hydrodynamic model has been employed to explore the mechanism of nonlocal feature on the nonlinear high order harmonic generation. In [2], an energy stable discontinuous Galerkin method has been designed for the Maxwell equations in Kerr-Raman-type nonlinear optical media for the simulation of third harmonic wave. Numerical investigations on the high order harmonic generation using a perturbation hydrodynamic model [32] and a fully hydrodynamic model [7,9] are also reported in literatures. Concerning the nonlocal effect, a mixed finite element method (FEM) adopting the Nédélec element has been developed in [10] for simulating the nonlocal effect of a groove and a nanowire by using a nonlocal hydrodynamic Drude model in the two-dimensional frequency domain. In [24], the authors developed an energy stable DGTD scheme to solve a linearized nonlocal dispersion model for studying the nonlocal dispersion effect from the interaction of light with nanometer scale metallic structures. In [29], the authors applied a hybridizable discontinuous Galerkin (HDG) method to solve the Maxwell equations coupled with the nonlocal hydrodynamic Drude model in the frequency domain for computing the nonlocal electromagnetic effect from a two-dimensional gold nanowire and a three-dimensional periodic annular nanogap structure.

In this paper, we employ a coupled system of the gas dynamic equations including the pressure term and the Maxwell equations (also named as the hydrodynamic electron fluid Maxwell equations (HEFMEs) in [33]) to simulate both the high-order harmonic generation and the nonlocal effect in metallic nanostructures using the high order Runge-Kutta discontinuous Galerkin (RKDG) method [6]. Analysis of an energy-stable discontinuous Galerkin (DG) method coupled with leap-frog or trapezoidal time discretization schemes for simulating nonlinear optical phenomenons has been discussed in [18]. We successfully simulate high-order harmonic generations from different arrays of periodically arranged metallic nanostructures. In addition, by a switch-on-and-off numerical examination on different nonlinear terms, we conclude that only the quantum pressure term is responsible for the nonlocal effects. In order to simulate the SHG from a metallic nanostructure adjacent to a nanostructure with some kind of non-metallic material, we couple the HEFMEs with an effective polarization model [23] to numerically investigate the influence of bound electrons on the generation of high order harmonics. A strengthened influence of bound electrons on the generation of high order harmonic waves associated to the numerical setting in this work has been successfully observed. A generalized Padé expansion model taking the bound electrons into account has been formerly studied in [25] in which a high order upwind DG scheme on unstructured grid has been proposed for numerical solutions.

In [9], Hille et al. developed a robust DG scheme with upwind numerical flux for Maxwell's equations and Lax-Friedrichs(LF) numerical flux for electron fluid equations to have a systematic numerical survey on the SHG based on the coupled system. However, it is well known that, among all commonly used exact or approximate Riemann solvers, the LF numerical flux will lead to much larger numerical errors than other exact or approximate Riemann solvers due to its large amount of numerical viscosity, therefore, for long time wave propagation problem, a more robust and efficient approximate Riemann solver is preferred. Here, inspired by the work in [22], we employ the Harten-Lax-van-Leer(HLL) numerical flux for the simulation and make a comparison between the numerical solutions using HLL numerical flux and those using the LF numerical flux. Numerical accuracy tests indicate that the HLL numerical flux produces a better performance that the LF flux during our simulations.

This paper is organized as follows. In Section 2, we introduce the mathematical governing equations, and then formulate in details the numerical scheme for solving the coupled system in Section 3. In Section 4, numerical tests on the nonlocal effect and the second harmonic generation are presented to show the efficiency of the model and numerical method. Conclusions are finally given in Section 5.

2. Mathematical model

2.1. Maxwell equations

The governing equations for the propagation of electromagnetic waves are the Maxwell equations

$$\mu_0 \frac{\partial \tilde{\mathbf{H}}}{\partial \tilde{t}} + \tilde{\nabla} \times \tilde{\mathbf{E}} = \mathbf{0}\,, \tag{1}$$

$$\epsilon_0 \frac{\partial \tilde{\mathbf{E}}}{\partial \tilde{t}} - \tilde{\nabla} \times \tilde{\mathbf{H}} = -\tilde{\mathbf{J}} - \tilde{\mathbf{J}}_b\,. \tag{2}$$

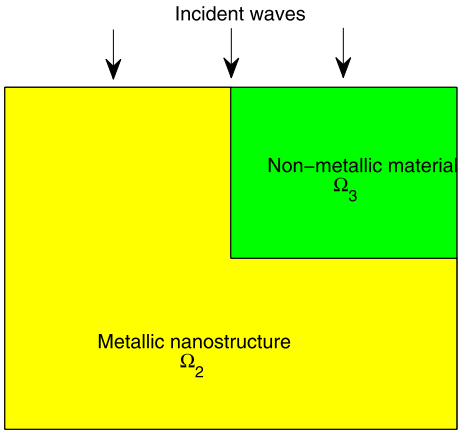

Fig. 1. Illustration for the nanostructure.

Here, ϵ_0, μ_0 are the permittivity and the permeability in free space, respectively, $\tilde{\mathbf{E}}$ is the electric field, $\tilde{\mathbf{H}}$ is the magnetic field, $\tilde{\mathbf{J}}$ denotes the current density generated by the motion of electrons in a metallic nanostructure and thus identically equals to zero outside the metallic nanostructure, and $\tilde{\mathbf{J}}_b$ is the bound current density which is trivial if the effect of bound electrons is neglected.

2.2. Gas dynamic equations

As being shown in Fig. 1, Ω_2 is a bounded domain occupied by a metallic nanostructure, which is excited by an external electromagnetic field. From continuum mechanics, the motion of free electrons in the metallic nanostructure Ω_2 satisfies the following Euler equations

$$\frac{\partial(\tilde{n}_e\tilde{q}_e)}{\partial\tilde{t}} + \tilde{\nabla}\cdot(\tilde{n}_e\tilde{q}_e\tilde{\mathbf{u}}_e) = 0\,, \tag{3}$$

$$\tilde{m}_e\left[\frac{\partial\tilde{\mathbf{u}}_e}{\partial\tilde{t}} + (\tilde{\mathbf{u}}_e\cdot\tilde{\nabla})\tilde{\mathbf{u}}_e\right] = \tilde{q}_e(\tilde{\mathbf{E}} + \mu_0\tilde{\mathbf{u}}_e\times\tilde{\mathbf{H}}) - \tilde{\gamma}\tilde{m}_e\tilde{\mathbf{u}}_e - \frac{\tilde{\nabla}\tilde{p}}{\tilde{n}_e}\,, \tag{4}$$

where $\tilde{q}_e, \tilde{m}_e, \tilde{n}_e, \tilde{\mathbf{u}}_e$ denote the electron charge, mass, number density and velocity field, respectively. $\tilde{\gamma} = 1/\tilde{\tau}$ denotes the relaxation time, the average time of collisions between the electrons and the ions. $\tilde{p} = (3\pi^2)^{2/3}(\hbar^2/5\tilde{m}_e)\tilde{n}_e^{5/3}$, with $\hbar$ being the Planck's constant, is the electron gas pressure evaluated by the Thomas-Fermi theory [20]. We name equations (1)-(4) as the HEFMEs which has been used in [9,33] for SHG simulations. Unlike the NHD in [16], the HEFMEs provides a nonlocal description of free electrons by adding additional quantum pressure term. With its inherent nonlinearity, one expects to be able to observe both the high-order harmonic generation and the nonlocal optical response in numerics using this self-consistent model.

2.3. Polarization model

Let Ω_3 (see Fig. 1) be a bounded domain filled with some kind of non-metallic material, being adjacent to Ω_2. In the domain Ω_3, the electrons are subject to the linear and nonlinear restoring forces and can not leave far away from their atomic nucleus. We call these electrons as the bound electrons. Let $\tilde{\mathbf{P}}$ be the polarization and $\tilde{\mathbf{J}}_b$ be the bound current density, respectively, an effective polarization model for bound charges can be obtained by using Newton's second law and neglecting the nonlinear restoring forces [23]

$$\frac{\partial\tilde{\mathbf{P}}}{\partial\tilde{t}} = \tilde{\mathbf{J}}_\mathbf{b}, \tag{5}$$

$$\frac{\partial\tilde{\mathbf{J}}_\mathbf{b}}{\partial\tilde{t}} + \tilde{\gamma}_b\tilde{\mathbf{J}}_\mathbf{b} + \tilde{\omega}_b^2\tilde{\mathbf{P}} = \frac{\tilde{n}_b\tilde{q}_e^2}{\tilde{m}_e}\tilde{\mathbf{E}} + \frac{\mu_0\tilde{q}_e}{\tilde{m}_e c}\tilde{\mathbf{J}}_\mathbf{b}\times\tilde{\mathbf{H}}\,. \tag{6}$$

Here, $\tilde{n}_b$, $\tilde{\gamma}_b$, $\tilde{\omega}_b$ denote the constant ion density, damping coefficient and resonance frequency for the bound electrons, respectively, and c denotes the speed of light in vacuum. We point out that this model defined on the domain Ω_3 is coupled with the HEFMEs for the numerical simulation only when we consider the numerical test on the influence of bound electrons (the last part in Section 4.2).

Table 1
Unit system.

Physical quantity	Reference scale	Redefined quantity
$\tilde{L}$	$L_0 = 1.0 \times 10^{-9} m$	$L = \tilde{L}/L_0$
$\tilde{t}$	$t_0 = L_0/c, c = 1/\sqrt{\mu_0 \epsilon_0}$	$t = \tilde{t}/t_0$
$\tilde{\nabla}$		$\nabla = L_0 \tilde{\nabla}$
$\partial/\partial\tilde{t}$		$\partial/\partial t = t_0 \partial/\partial\tilde{t}$
$\tilde{\mathbf{E}}$	$E_0 = 1.0 \times 10^7 V/m$	$\mathbf{E} = \tilde{\mathbf{E}}/E_0$
$\tilde{\mathbf{H}}$	$H_0 = E_0/Z, Z = \sqrt{\mu_0/\epsilon_0}$	$\mathbf{H} = \tilde{\mathbf{H}}/H_0$
$\tilde{\mathbf{J}}$	$J_0 = E_0/(ZL_0)$	$\mathbf{J} = \tilde{\mathbf{J}}/J_0$
$\tilde{\mathbf{J}}_b$	J_0	$\mathbf{J}_b = \tilde{\mathbf{J}}_b/J_0$
$\tilde{\mathbf{P}}$	$t_0 J_0$	$\mathbf{P} = \tilde{\mathbf{P}}/(t_0 J_0)$
$\tilde{\rho}$	$\rho_0 = \epsilon_0/L_0$	$\rho = \tilde{\rho}/\rho_0$
$\tilde{\omega}$	$\omega_0 = c/L_0$	$\omega = \tilde{\omega}/\omega_0$

2.4. Compact nondimensionalized forms

In this paper, we will investigate the nonlinear and nonlocal responses in numerics based on the HEFMEs. As pointed out in [24], a simple 2D TE mode modeling is sufficient to produce the bulk plasmons for inducing the nonlocal effect. Concerning the nonlinear responses such as the high order harmonic generation, the nonlinearity in the 2D HEFMEs in TE mode is not adequate, and a full 3D simulation is preferred for numerical simulations. As a compromise in the current work, we make an assumption of z-invariance for the materials to be considered which implies that the metamaterials are uniformly infinitely arranged along the z axis. The following notation for the curl operator is used for the vector field $\mathbf{u} = (u_x, u_y, u_z)$:

$$\nabla \times \mathbf{u} = \left(\frac{\partial u_z}{\partial y}, -\frac{\partial u_z}{\partial x}, \frac{\partial u_y}{\partial x} - \frac{\partial u_x}{\partial y} \right)^\top .$$

Assume that $\Omega_1 \subset \mathbb{R}^2$ is a finite truncation enclosing $\Omega_2 \cup \Omega_3$ inside. By defining the charge density $\tilde{\rho}$ and the current density $\tilde{\mathbf{J}}$ as follows

$$\tilde{\rho} = \tilde{n}_e \tilde{q}_e , \qquad \tilde{\mathbf{J}} = \tilde{\rho} \tilde{\mathbf{u}}_e ,$$

we can write the equations (1)-(2) and (3)-(4) in the following compact hyperbolic system after a nondimensionalization procedure according to Table 1

$$\frac{\partial U_1}{\partial t} + \nabla \cdot \boldsymbol{F}_1(U_1) = S_1(U_2, U_3), \text{ in } \Omega_1 \times [0, T] , \tag{7}$$

$$\frac{\partial U_2}{\partial t} + \nabla \cdot \boldsymbol{F}_2(U_2) = S_2(U_1, U_2), \text{ in } \Omega_2 \times [0, T], \tag{8}$$

where $\boldsymbol{F}_1(U_1) = (F_1(U_1), G_1(U_1))$, $\boldsymbol{F}_2(U_2) = (F_2(U_2), G_2(U_2))$. We could also formulate the polarization model into the following compact ordinary differential system according to Table 1

$$\frac{dU_3}{dt} = S_3(U_1, U_3), \text{ in } \Omega_3 \times [0, T] . \tag{9}$$

In the above formulations,

$$U_1 = \begin{pmatrix} H_x \\ H_y \\ H_z \\ E_x \\ E_y \\ E_z \end{pmatrix}, F_1(U_1) = \begin{pmatrix} 0 \\ -E_z \\ E_y \\ 0 \\ H_z \\ -H_y \end{pmatrix}, G_1(U_1) = \begin{pmatrix} E_z \\ 0 \\ -E_x \\ -H_z \\ 0 \\ H_x \end{pmatrix}, S_1 = -\begin{pmatrix} 0 \\ 0 \\ 0 \\ \rho u_x + J_{bx} \\ \rho u_y + J_{by} \\ \rho u_z + J_{bz} \end{pmatrix}$$

$$U_2 = \begin{pmatrix} \rho \\ \rho u_x \\ \rho u_y \\ \rho u_z \end{pmatrix}, F_2(U_2) = \begin{pmatrix} \rho u_x \\ \rho u_x u_x + k\rho^{5/3} \\ \rho u_x u_y \\ \rho u_x u_z \end{pmatrix}, G_2(U_2) = \begin{pmatrix} \rho u_y \\ \rho u_x u_y \\ \rho u_y u_y + k\rho^{5/3} \\ \rho u_x u_z \end{pmatrix},$$

$$k=\frac{1}{5}\left(\frac{\hbar}{m_e}\right)^2\left(\frac{3\pi^2}{q_e}\right)^{2/3},\ S_2=\begin{pmatrix}0\\ \frac{\rho q_e}{m_e}(E_x+u_yH_z-u_zH_y)-\gamma\rho u_x\\ \frac{\rho q_e}{m_e}(E_y+u_zH_x-u_xH_z)-\gamma\rho u_y\\ \frac{\rho q_e}{m_e}(E_z+u_xH_y-u_yH_x)-\gamma\rho u_z\end{pmatrix},$$

$$U_3=\begin{pmatrix}P_x\\ P_y\\ P_z\\ J_{bx}\\ J_{by}\\ J_{bz}\end{pmatrix},\ S_3=\begin{pmatrix}J_{bx}\\ J_{by}\\ J_{bz}\\ \frac{n_bq_e^2}{m_e}E_x+\frac{q_e}{m_e}(J_{by}H_z-J_{bz}H_y)-\gamma_bJ_{bx}-\omega_b^2P_x\\ \frac{n_bq_e^2}{m_e}E_y+\frac{q_e}{m_e}(J_{bz}H_x-J_{bx}H_z)-\gamma_bJ_{by}-\omega_b^2P_y\\ \frac{n_bq_e^2}{m_e}E_z+\frac{q_e}{m_e}(J_{bx}H_y-J_{by}H_x)-\gamma_bJ_{bz}-\omega_b^2P_z\end{pmatrix},$$

T is the final simulation time, and the subscript x (y or z) denotes the x (y or z) component of corresponding unknowns.

3. Numerical schemes

In this section, we will present the numerical method solving the equations (7)-(9). Let $\mathscr{T}_h$ be a partition of Ω_1. For each element $K\in\mathscr{T}_h$, we define the following finite dimensional discrete spaces consisting of piecewise polynomials with the degree at most k

$$V^p_{h,\Omega_1}:=\{U\in\left(L^2(\Omega_1)\right)^p:U|_K\in\left(P^k(K)\right)^p,\forall K\in\mathscr{T}_h\},$$
$$W^q_{h,\Omega_2}:=\{U\in\left(L^2(\Omega_2)\right)^q:U|_K\in\left(P^k(K)\right)^q,\forall K\in\tilde{\mathscr{T}}_h\},$$
$$V^p_{h,\Omega_3}:=\{U\in\left(L^2(\Omega_3)\right)^p:U|_K\in\left(P^k(K)\right)^p,\forall K\in\hat{\mathscr{T}}_h\},$$

where $\tilde{\mathscr{T}}_h=\{K\in\mathscr{T}_h:K\subset\Omega_2\}$, and $\hat{\mathscr{T}}_h=\{K\in\mathscr{T}_h:K\subset\Omega_3\}$. We assume that the boundary of each subdomain Ω_i, $i=1,2,3$, belongs to the set of boundary of K, or contains the vertex nodes of K.

3.1. Schemes with the forward Euler time discretization

We start introducing the schemes with the first order forward Euler method for the time discretization, and the higher order time discretization will be discussed in Section 3.2. The proposed schemes evolve the numerical solutions U_{1h}, U_{2h} and U_{3h}, which are assumed to be available at $t=t^n$, denoted by $U^n_{1h}\in V^6_{h,\Omega_1}$, $U^n_{2h}\in W^4_{h,\Omega_2}$ and $U^n_{3h}\in V^6_{h,\Omega_3}$, and will be computed at $t=t^{n+1}=t^n+\Delta t^n$, denoted by U^{n+1}_{1h}, U^{n+1}_{2h} and U^{n+1}_{3h}.

3.1.1. Updating U^{n+1}_{1h}

To get U^{n+1}_{1h}, we apply to (7) with the DG method for the space discretization and the first order forward Euler method for the time discretization. That is, to look for $U^{n+1}_{1h}\in V^6_{h,\Omega_1}$, for $\forall\,\Phi_h\in V^6_{h,\Omega_1}$ and $\forall K\in\mathscr{T}_h$, such that

$$\int_K U^{n+1}_{1h}\cdot\Phi_h d\boldsymbol{x}=\int_K U^n_{1h}\cdot\Phi_h d\boldsymbol{x}+\Delta t^n\int_K\mathbf{F}_1(U^n_{1h})\cdot\nabla\Phi_h d\boldsymbol{x}$$
$$-\Delta t^n\int_{\partial K}\mathcal{H}_1(U^{n,int}_{1h},U^{n,ext}_{1h})\cdot\Phi_h dS+\Delta t^n\int_K S_1(U^n_{2h},U^n_{3h})\cdot\Phi_h d\boldsymbol{x},\tag{10}$$

where $\mathcal{H}_1(\cdot,\cdot)$ denotes the numerical flux evaluated on the interface between two adjacent elements, and $U^{n,int}_{1h}$, $U^{n,ext}_{1h}$ are the traces of U^n_{1h} on ∂K evaluated from the interior and exterior of element K. In this paper, we employ the upwind(UW) numerical flux [17] given by

$$\mathcal{H}_1(U^{n,int}_{1h},U^{n,ext}_{1h})=\begin{pmatrix}\boldsymbol{n}_K\times\frac{(Y\boldsymbol{E}-\boldsymbol{n}_K\times\boldsymbol{H})^{n,int}_h+(Y\boldsymbol{E}+\boldsymbol{n}_K\times\mathbf{H})^{n,ext}_h}{Y^{n,int}_h+Y^{n,ext}_h}\\ -\boldsymbol{n}_K\times\frac{(Z\boldsymbol{H}+\boldsymbol{n}_K\times\boldsymbol{E})^{n,int}_h+(Z\boldsymbol{H}-\boldsymbol{n}_K\times\mathbf{E})^{n,ext}_h}{Z^{n,int}_h+Z^{n,ext}_h}\end{pmatrix},$$

where $Z=\frac{1}{Y}=\sqrt{\frac{\mu}{\epsilon}}$ denotes the local impedance, and $\boldsymbol{n}_K$ denotes the unit outward normal of K.

3.1.2. Updating U_{2h}^{n+1} and U_{3h}^{n+1}

To get U_{2h}^{n+1}, we apply to (8) with the DG method for the space discretization and the first order forward Euler method for the time discretization. That is, to look for $U_{2h}^{n+1} \in W_{h,\Omega_2}^4$, for $\forall\, \Psi_h \in W_{h,\Omega_2}^4$ and $\forall K \in \tilde{\mathscr{T}}_h$, such that

$$\int_K U_{2h}^{n+1} \cdot \Psi_h d\boldsymbol{x} = \int_K U_{2h}^{n} \cdot \Psi_h d\boldsymbol{x} + \Delta t^n \int_K \mathbf{F}_2(U_{2h}^n) \cdot \nabla \Psi_h d\boldsymbol{x} - \Delta t^n \int_{\partial K} \mathcal{H}_2(U_{2h}^{n,int}, U_{2h}^{n,ext}) \cdot \Psi_h dS + \Delta t^n \int_K S_2(U_{1h}^n, U_{2h}^n) \cdot \Psi_h d\boldsymbol{x}\,, \tag{11}$$

where $\mathcal{H}_2(\cdot,\cdot)$ denotes the numerical flux evaluated on the interface between two adjacent elements, and $U_{2h}^{n,int}$, $U_{2h}^{n,ext}$ are the traces of U_{2h}^n on ∂K evaluated from the interior and exterior of element K. In [9], the following Lax-Friedrichs (LF) numerical flux is employed:

$$\mathcal{H}_2^{LF}(U_{2h}^{n,int}, U_{2h}^{n,ext}) = \frac{1}{2}\left[\boldsymbol{F}_2(U_{2h}^{n,int}) \cdot \boldsymbol{n}_K + \boldsymbol{F}_2(U_{2h}^{n,ext}) \cdot \boldsymbol{n}_K - \alpha^n \left(U_{2h}^{n,ext} - U_{2h}^{n,int}\right)\right],$$

where, α^n is taken as the absolute value of eigenvalues in the direction $\boldsymbol{n}_K$ of the hyperbolic system. However, as pointed out in [22], among the commonly employed exact or approximate Riemann solvers, the Lax-Friedrichs numerical flux introduces a relatively large amount of numerical viscosity, therefore, for long time wave simulation, a more robust Riemann solver is preferred. In this paper, we adopt the Harten-Lax-van Leer (HLL) numerical flux:

$$\mathcal{H}_2^{HLL}(U_{2h}^{n,int}, U_{2h}^{n,ext}) = \begin{cases} \boldsymbol{F}(U_{2h}^{n,int}) \cdot \boldsymbol{n}_K & \text{if} \quad 0 \le S^{int}, \\ \frac{S^{ext}\boldsymbol{F}(U_{2h}^{n,int})\cdot\boldsymbol{n}_K - S^{int}\boldsymbol{F}(U_{2h}^{n,ext})\cdot\boldsymbol{n}_K + S^{int}S^{ext}(U_{2h}^{n,ext} - U_{2h}^{n,int})}{S^{ext} - S^{int}} & \text{if} \quad S^{int} < 0 < S^{ext}, \\ \boldsymbol{F}(U_{2h}^{n,ext}) \cdot \boldsymbol{n}_K & \text{if} \quad S^{ext} \le 0, \end{cases}$$

where, S^{int} and S^{ext} are simply taken as [30]

$$S^{int} = \min(V^{int} - c_f^{int}, V^{ext} - c_f^{ext}), c_f^{int} = \sqrt{\frac{5}{3}\kappa {\rho^{int}}^{2/3}}, \tag{12}$$

$$S^{ext} = \min(V^{int} + c_f^{int}, V^{ext} + c_f^{ext}), c_f^{int} = \sqrt{\frac{5}{3}\kappa {\rho^{ext}}^{2/3}} \tag{13}$$

where V^{int} and V^{ext} are the velocity components of the interior and exterior states with respect to the cell boundary ∂K. More advanced approximate Riemann solver, for example, an entropy stable numerical flux for the HEFMEs will be explored in the future work.

Since (9) is an system of ordinary differential equations, with the first order forward Euler method we look for $U_{3h}^{n+1} \in V_{h,\Omega_3}^6$, such that

$$U_{3h}^{n+1} = U_{3h}^n + \Delta t^n S_3(U_{1h}^n, U_{3h}^n)\,. \tag{14}$$

3.2. Schemes with high order time discretizations

In the previous subsection, we have only discussed the first order forward Euler time discretization. To match the high order accurate spatial DG discretization, the high order temporal discretizations will be used in the numerical implementation. Due to the presence of strong nonlinearity and complicated magneto-hydrodynamic coupling in this context, the HEFMEs admit discontinuous solutions, and the nonphysical numerical oscillations may induce the blow-up of the simulation. In [8], Gottlieb et al. proposed a strong stability preserving high-order time discretization scheme which is stable in any norm and ensures total-variation-diminishing (TVD) numerical solutions. In this paper, we choose the third order TVD Runge-Kutta method

$$\begin{aligned} U^{(1)} &= U^n + \Delta t_n \mathcal{L}(U^n) \\ U^{(2)} &= \frac{3}{4}U^n + \frac{1}{4}(U^{(1)} + \Delta t_n \mathcal{L}(U^{(1)})) \\ U^{n+1} &= \frac{1}{3}U^n + \frac{2}{3}(U^{(2)} + \Delta t_n \mathcal{L}(U^{(2)}))\,. \end{aligned} \tag{15}$$

We point out finally that the scheme (15) is a convex combination of the forward Euler time discretization.

3.3. Numerical ingredients

Numerical investigations on complex optical phenomena are closely related to numerical settings. In this subsection, we will describe in details numerical ingredients, including the initial conditions, and the interface and absorbing boundary conditions, etc.

3.3.1. Initial conditions

Before excited by the electromagnetic fields, the electrons in the nanostructures are at rest if the thermal effect is ignored. Under this circumstance, the electron number density is equal to the ion number density n_0 so that nanostructures are electrically neutral, where n_0 could be evaluated via the plasma frequency $\omega_p = \sqrt{\frac{n_0 q_e^2}{m_e}}$. Therefore, the initial conditions are set as follows

$$\mathbf{E}(\boldsymbol{x}, 0) = \mathbf{H}(\boldsymbol{x}, 0) = \mathbf{0}, \text{ in } \Omega_1 ,$$
$$\rho(\boldsymbol{x}, 0) = q_e n_0, \ \mathbf{u}(\boldsymbol{x}, 0) = \mathbf{0}, \text{ in } \Omega_2 ,$$
$$\mathbf{P}(\boldsymbol{x}, 0) = \mathbf{J}_b(\boldsymbol{x}, 0) = \mathbf{0}, \text{ in } \Omega_3 .$$

3.3.2. Boundary conditions on $\Gamma_2 = \partial\Omega_2$

In order to solve the HEFMEs, two boundary conditions need to be prescribed, one of which is the boundary condition on the metal surface $\Gamma_2 = \partial\Omega_2$. At the microscopic level, the charge density ρ varies continuously across the dielectric-metal interface, and there is actually a transition region with a scale of a few atomic diameters where the charge density changes gradually down to be trivial [28,16]. However, the thickness of the transition layer is a negligible scale compared to the finest mesh that we are able to afford in domain discretizations. This fact makes it impossible for us to implement the ab-*initio* boundary condition in a macroscopic model [11]. We use a natural boundary condition in this work, namely $\frac{\partial \rho}{\partial \boldsymbol{n}} = 0$. For the current density $\mathbf{J}$, we employ the so-called *slip* boundary condition, i.e. $\mathbf{n} \cdot \mathbf{J} = 0$. It implies that the current density is prohibited to travel out of the nanoparticle surface in a normal direction with respect to the interface while a tangential current shift is allowed. For the coupled polarization model, we do not need to specify any boundary conditions as the governing equations are a set of ordinary differential equations.

3.3.3. Artificial boundary conditions on $\Gamma_1 = \partial\Omega_1$

We need to employ an artificial boundary enclosing $\Omega_2 \cup \Omega_3$, denoted by $\Gamma_1 = \partial\Omega_1$, for the practical computation. We claim that there is no intersection between Γ_1 and the boundary of $\Omega_2 \cup \Omega_3$. In this paper, we use the uniaxial perfectly matched layer (PML) [17] to absorb the electromagnetic waves propagating through the boundary Γ_1 except for those tests with particular specifications. Let Ω_p be the PML region (see Fig. 2) surrounding the finite truncation Ω_1, and the modified formulations for (7) in Ω_p are written as

$$\frac{\partial U_1}{\partial t} + \nabla \cdot \boldsymbol{F}_1(U_1) = S_p(U_1, U_7), \text{ in } \Omega_p \times [0, T] , \tag{16}$$

and

$$\frac{dU_7}{dt} = S_7, \text{ in } \Omega_p \times [0, T] , \tag{17}$$

where

$$S_p = \begin{pmatrix} Q_x + (\sigma_x - \sigma_y)H_x \\ Q_y + (\sigma_y - \sigma_x)H_y \\ Q_z - (\sigma_x + \sigma_y)H_z \\ P_x + (\sigma_x - \sigma_y)E_x \\ P_y + (\sigma_y - \sigma_x)E_y \\ P_z - (\sigma_x + \sigma_y)E_z \end{pmatrix}, \ U_7 = \begin{pmatrix} Q_x \\ Q_y \\ Q_z \\ P_x \\ P_y \\ P_z \end{pmatrix}, \ S_7 = \begin{pmatrix} -\sigma_x Q_x - \sigma_x(\sigma_x - \sigma_y)H_x \\ -\sigma_y Q_y - \sigma_y(\sigma_y - \sigma_x)H_y \\ -\sigma_x\sigma_y H_z \\ -\sigma_x P_x - \sigma_x(\sigma_x - \sigma_y)E_x \\ -\sigma_y P_y - \sigma_y(\sigma_y - \sigma_x)E_y \\ -\sigma_x\sigma_y E_z \end{pmatrix}.$$

Here, the parameters of the dissipative layer for absorbing the fields propagating in the i-th direction σ_i are given by

$$\sigma_i = \sigma_m \left(\frac{d_i}{\delta}\right)^n , \ i = x, y ,$$

where d_i, δ, n denote the distance from the PML-vacuum interface, the thickness of PML, and the degree of polynomials, respectively. σ_m is the maximum electric conductivity which can be determined by

$$R(0) = e^{-2\sigma_m \delta/(n+1)} ,$$

where $R(0)$ denotes the theoretical reflection at normal incidence. The equations (16)-(17) are solved by the RKDG method as well.

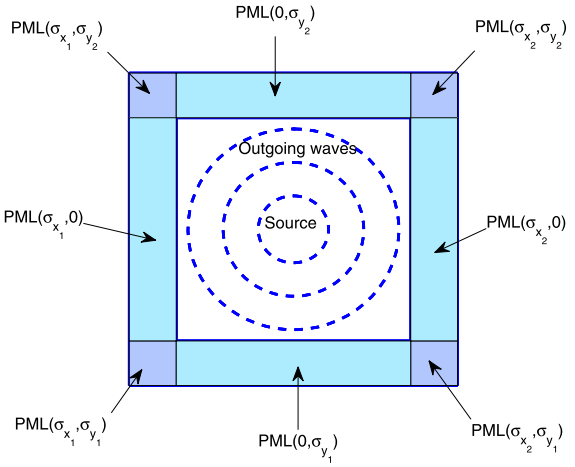

Fig. 2. Perfectly matched layer.

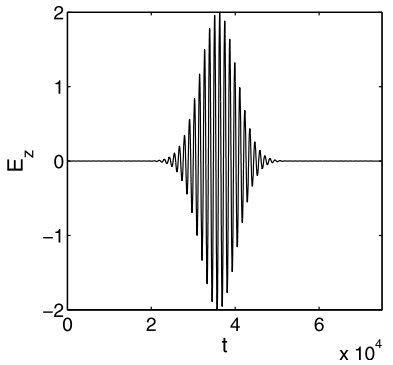

Fig. 3. Gaussian pulse: $E_A = 2.0$, $\lambda_0 = 1200$, $t_d = 3.598 \times 10^4$, $t_b = 0.6t_d$.

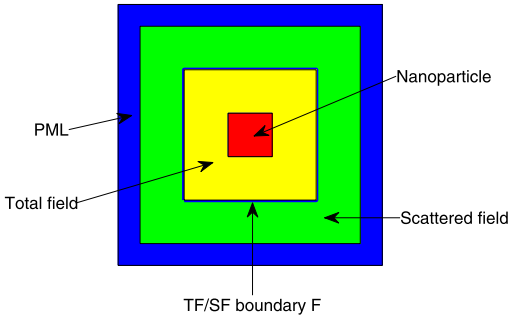

Fig. 4. Total-field and Scattered-field.

3.3.4. TF/SF technique

In order to stimulate the plasmon resonances in the metallic nanostructures, the initial conditions presented in 3.3.1 are not sufficient, and an extra appropriate wave source should be added during the computation. In this paper, we take the incident wave as a z-polarized Gaussian pulse modulated by the sine function

$$E_z = E_A \sin(\omega_m t) e^{(-\frac{4\pi(t-t_d)^2}{t_b^2})}, \ \omega_m = \frac{2\pi}{\lambda_0},$$

where λ_0 is the carrier center wavelength, E_A is the peak amplitude, t_d is the pulse duration, and t_b is the optical bandwidth (see Fig. 3). To implement this source injection in simulations, since the popular method of hard source in computational electromagnetics may produce backward-scattered waves in a longtime simulation, we apply in this work the total-field/scattered-field (TF/SF) technique [27] which requires to divide the computational domain into a total-field

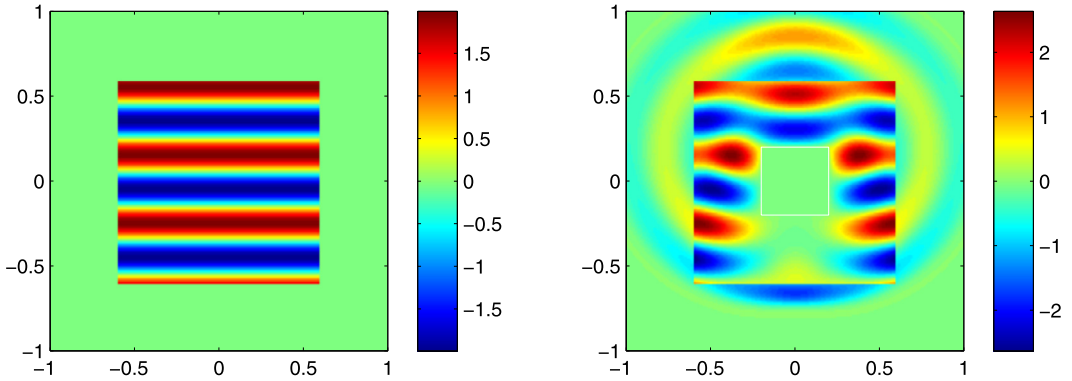

Fig. 5. Injection of sine plane wave via TF/SF, Left: Electric field E_z without object. Right: Electric field E_z with a square perfect electric conductor in total zone. (For interpretation of the colors in the figure(s), the reader is referred to the web version of this article.)

zone and a scattered-field zone (see Fig. 4) through a virtual TF/SF boundary F inside Γ_1. An incident wave is then introduced into the total-field zone from the virtual boundary without introducing any nonphysical effects. Meanwhile, a simple process on numerical fluxes along the virtual boundary allows us to realize this purpose efficiently and accurately (see Fig. 5).

4. Numerical results

We present in this section numerical results which are computed based on the coupling system of (7)-(8) ($\boldsymbol{J}_b = 0$ and Ω_3 is empty) except for the last case in Section 4.2 where we compute the HEFMEs (7)-(8) together with the polarization model (9). In addition, all the simulations are performed with $P^k (k = 1, 2 \text{ or } 3)$ elements on structured grids, and if not specified, only numerical results approximated by fourth-order P^3 elements are presented for illustration. All physical parameters and numerical results, including the dimensions of nanostructures, are shown in nondimensionalized units. The time step Δt is dynamically determined by

$$\Delta t = \frac{C_{cfl}}{\frac{a_x}{\Delta x} + \frac{a_y}{\Delta y}},$$

where $a_x = \max(|u_x| + c^f, 1.0)$, $a_y = \max(|u_y| + c^f, 1.0)$, $c^f = \sqrt{\frac{5}{3} k |\rho|^{\frac{2}{3}}}$, C_{cfl} is the CFL number taken as $0.3, 0.18$ and 0.1 for $k = 1, k = 2$ and $k = 3$ respectively.

4.1. Accuracy test

We start with a manufactured example to study the accuracy of the RKDG with two different numerical fluxes, termed as RKDG-UW-LF and RKDG-UW-HLL respectively. We take $k = 0.8$, $\frac{q_e}{m_e} = 1, \gamma = 0.05$ in the equations (7) and (8) and employ the following functions as the manufactured solutions

$$\begin{cases} \rho &= 1 + 0.5\sin[2\pi(x + y - 2t)] \\ u_x &= 1 \\ u_y &= 1 \\ u_z &= 0 \\ H_x &= 0 \\ H_y &= 0 \\ H_z &= \cos(2\pi x)\cos(2\pi y)\sin(4\pi\alpha t) \\ E_x &= \alpha\cos(2\pi x)\sin(2\pi y)\cos(4\pi\alpha t) \\ E_y &= -\alpha\sin(2\pi x)\cos(2\pi y)\cos(4\pi\alpha t) \\ E_z &= 0 \end{cases}$$

where $\alpha = \frac{\sqrt{2}}{2}$. The computational domain is $\Omega_2 = \Omega_1 = [0, 1] \times [0, 1]$. Periodic boundary conditions are applied in both $x-$ and y-directions. In this experiment, the CFL numbers are taken as 0.3 and 0.18 for $k = 1$ and $k = 2$, while for $k = 3$, to maintain fourth-order accuracy in time, the time step is further restricted as $d\tau = dt^{4/3}$ with $C_{cfl} = 0.3$. In Table 2, we list

Table 2
Error table for ρ approximated by P^1, P^2 and P^3 element at $T = 1.0$ with LF numerical flux (left) and HLL numerical flux (right).

Mesh	$UW-LF$				$UW-HLL$			
	L^2 error	Order	L^∞ error	Order	L^2 error	Order	L^∞ error	Order
P^1								
10×10	3.50E-02	–	1.95E-01	–	2.03E-02	–	1.14E-01	–
20×20	8.74E-03	2.00	4.89E-02	2.00	4.37E-03	2.22	2.84E-02	2.00
40×40	2.20E-03	1.99	1.20E-02	2.03	1.02E-03	2.09	7.19E-03	1.98
80×80	5.51E-04	2.00	2.94E-03	2.03	2.53E-04	2.02	1.83E-03	1.98
160×160	1.38E-04	2.00	7.28E-04	2.01	6.28E-05	2.01	4.57E-04	2.00
P^2								
10×10	5.78E-03	–	4.00E-02	–	2.11E-03	–	1.64E-02	–
20×20	7.11E-04	3.02	5.59E-03	2.84	2.50E-04	3.07	2.05E-03	3.00
40×40	8.34E-05	3.09	6.83E-04	3.03	3.00E-05	3.06	2.55E-04	3.01
80×80	1.02E-05	3.03	8.50E-05	3.01	3.71E-06	3.02	3.16E-05	3.01
160×160	1.30E-06	2.97	1.08E-05	2.98	4.63E-07	3.00	3.91E-06	3.01
P^3								
10×10	3.40E-04	–	3.48E-03	–	1.68E-04	–	1.97E-03	–
20×20	2.86E-05	3.57	2.97E-04	3.55	1.08E-05	3.97	1.27E-04	3.96
40×40	2.07E-06	3.79	2.03E-05	3.87	6.88E-07	3.97	7.96E-06	4.00
80×80	1.36E-07	3.93	1.31E-06	3.96	4.24E-08	4.02	5.73E-07	3.80
160×160	8.61E-09	3.98	8.16E-08	4.00	2.64E-09	4.00	3.50E-08	4.03

the errors and the corresponding order of accuracy for ρ at $T = 1.0$. It shows that both schemes lead to optimal accuracy for P^k approximations with $k = 1, 2, 3$. However, due to the fact that the LF numerical flux is more dissipative, the numerical results in terms of LF numerical flux indicate a larger value on errors than those in term of the HLL numerical flux.

4.2. High-order harmonic generation

The high-order harmonic generation is a nonlinear optical process sensitive to the configurations of metallic nanostructures. In this test, we simulate the high-order harmonic generation from two typical metallic nanostructures, namely, an array of rectangular nanostructures (see the left of Fig. 6) and an array of L-shaped nanostructures (see the middle of Fig. 6). In addition, we also consider an array of L-shaped nanostructures with metallic materials and an array of rectangular nanostructures with non-metallic materials (see the right of Fig. 6) for purpose of studying the influence of bound electrons on the generation of high order harmonic waves. In our simulations, the nanostructures are arranged periodically in x-direction with plasma frequency $\omega_p = 4.560 \times 10^{-2}$, and $\gamma = 2.160 \times 10^{-4}$. For simplicity, we only focus on one single structure by using periodic boundary condition in x-direction and PML in y-direction [16]. Measurements on the linear response and the SHG signal can be computed in terms of the integrals of the electric fields E_z and E_x along the probing line S as follows

$$\hat{E}_{Linear} = \frac{1}{|S|}\int_S E_z ds\,,$$

$$\hat{E}_{SHG} = \frac{1}{|S|}\int_S E_x ds\,.$$

We employ an uniform mesh $\Delta x = \Delta y = 2.0$ in the simulation and the final time $T = 1.499 \times 10^5$. Based on the accuracy study in section 4.1, we provide numerical results obtained by both the RKDG-UW-LF scheme and the RKDG-UW-HLL scheme.

Firstly, we study the high order harmonic generation from the rectangular metallic nanostructures whose dimension is shown in Fig. 6 (Left). In Fig. 7, we plot the time history of linear response and SHG. As being shown in Fig. 7, there is no SHG from the rectangular metallic particle. This result is reasonable since the rectangular metallic nanostructure possesses a perfect centrosymmetric property which leads to a vanishing second-order nonlinear optical susceptibility tensor $\chi^{(2)}$ prohibiting the SHG. However, the rectangular metallic nanostructure does allow for the third harmonic generation (THG) since the symmetric property would not remove the third-order nonlinear optical susceptibility tensor $\chi^{(3)}$. In Fig. 8 (Left), spectrums of these responses are presented. In order to show the spectrums apparently, a zoom-in plot of the spectrum is presented in Fig. 8 (Right). It can be observed that, the third-order harmonic generation (400), the fifth-order harmonic generation (240) and the seventh-order harmonic generation (171.4) are captured in the simulation. We observe that there is no significant difference between the results attained by RKDG-UW-LF scheme and RKDG-UW-HLL scheme, respectively.

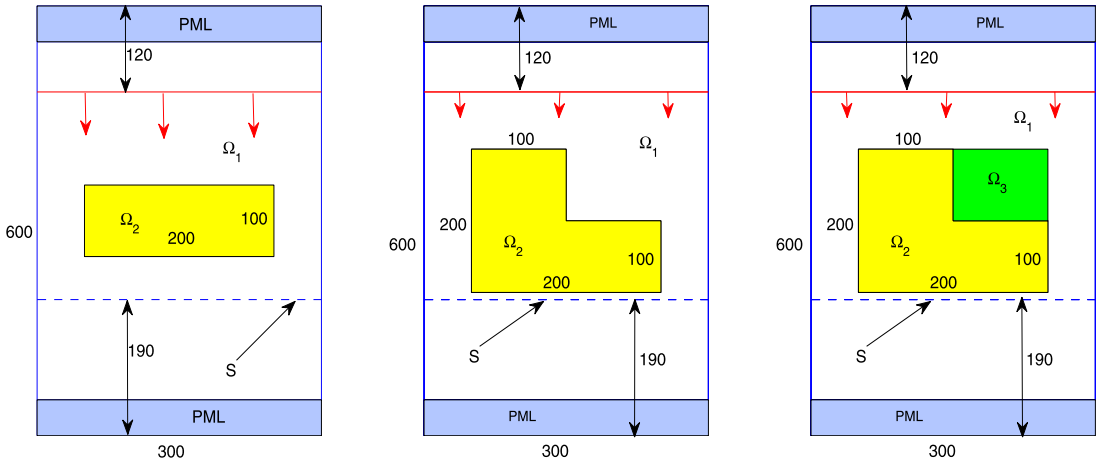

Fig. 6. Setup for simulations of high-order harmonic generations. Left: rectangular metallic nanostructure; middle: L-shaped metallic nanostructure; right: L-shaped metallic nanostructure adjacent to a rectangular non-metallic nanostructure.

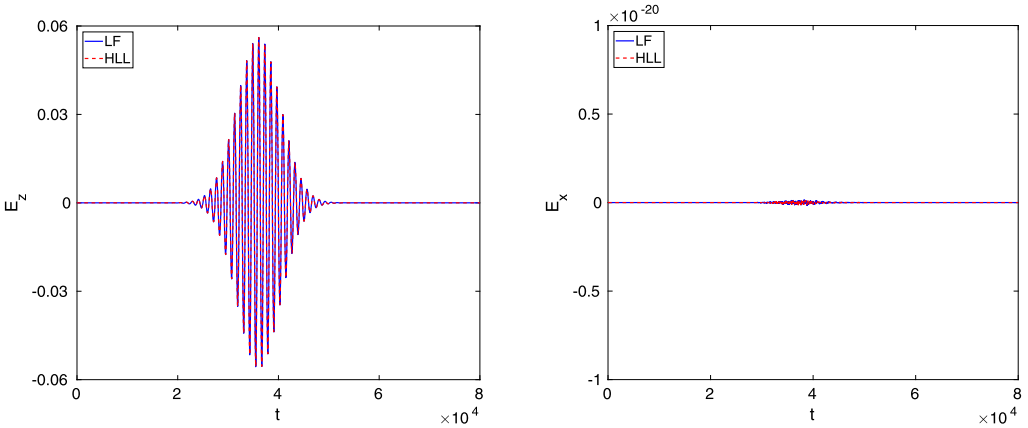

Fig. 7. Time history of electric fields from a rectangular nanostructure.

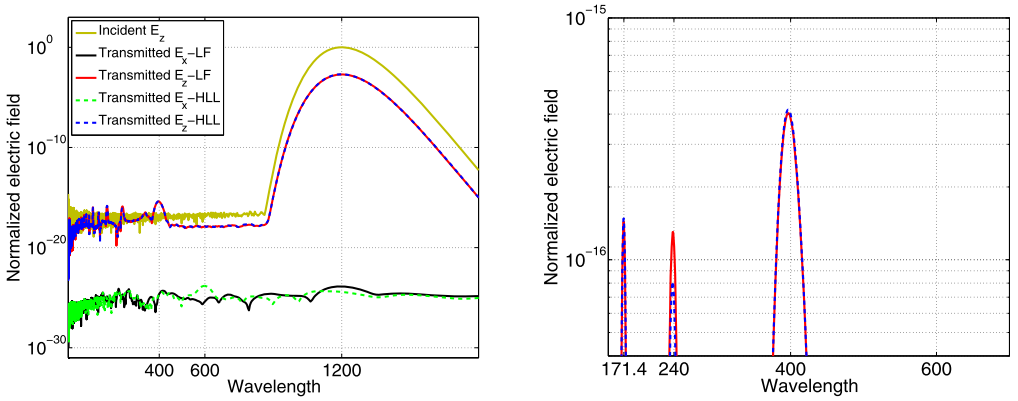

Fig. 8. Spectrum with a rectangular nanostructure. Left: Spectrum of incident wave E_z, transmitted wave E_x, E_z; right: Zoom-in plot of the spectrum.

Then, we take an investigation on the high order harmonic generation from the L-shaped metallic nanostructures (see Fig. 6 (middle) for the setup). In Fig. 9, we plot the time history of the linear response and the SHG. In Fig. 10 (Left), spectrums of these responses are presented. Since the centrosymmetry is broken in this case, the second order harmonic generation appears. As we can see from Fig. 10 that the fundamental wave (1200) can be frequency-doubled after propagating through the nanostructure, and the higher order harmonic waves, such as the third-order harmonic generation (400),

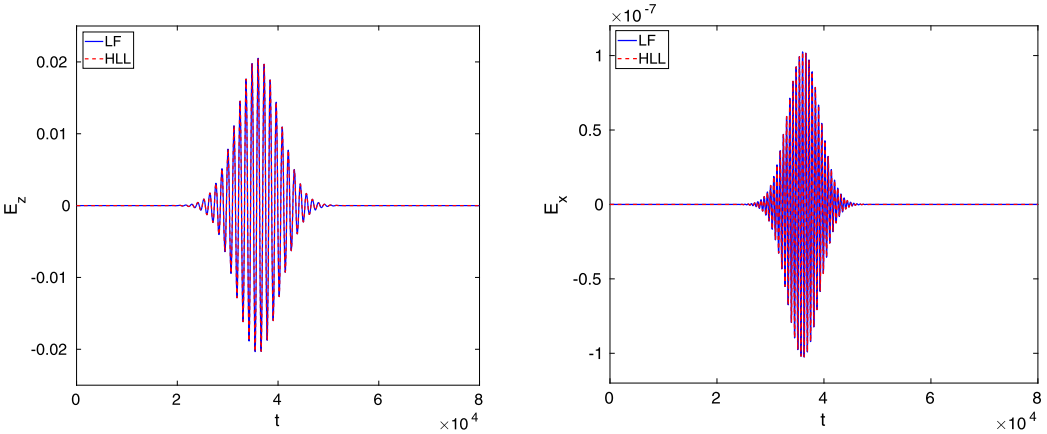

Fig. 9. Time history of electric fields from a L-shaped nanostructure.

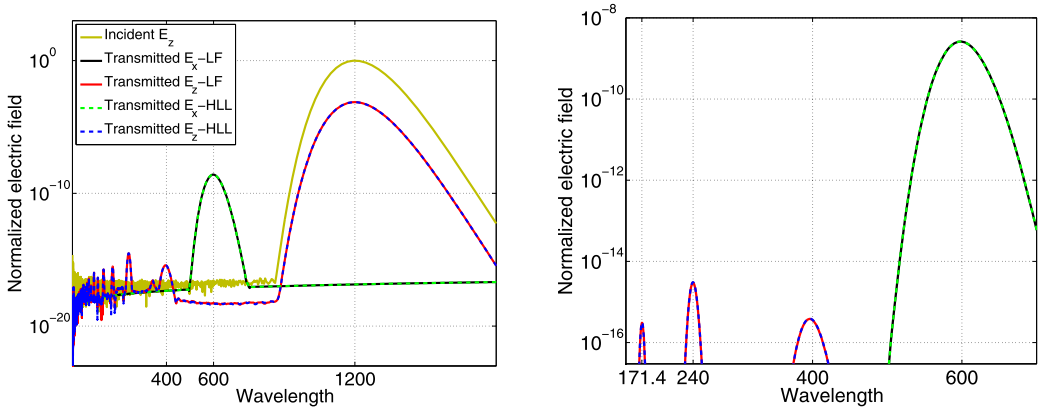

Fig. 10. Spectrum with an L-shaped nanostructure. Left: Spectrum of incident wave E_z, transmitted wave E_x, E_z; right: Zoom-in plot of the spectrum.

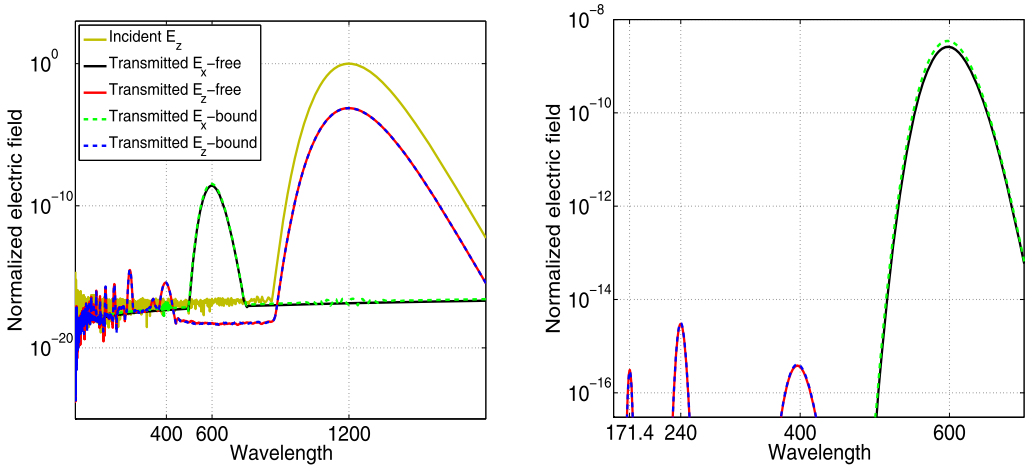

Fig. 11. Spectrum from a nanostructure with bound electrons. Left: Spectrum of transmitted wave E_x, E_z; right: Zoom-in plot of the spectrum.

the fifth-order harmonic generation (240) and the seventh-order harmonic generation (171.4) in the transmitted E_z, are also captured in the simulation. The above results associated with both the rectangular and the L-shaped metallic nanostructures are in a good agreement with those presented in [16]. Again, no significant difference between the results obtained by two DG schemes is observed.

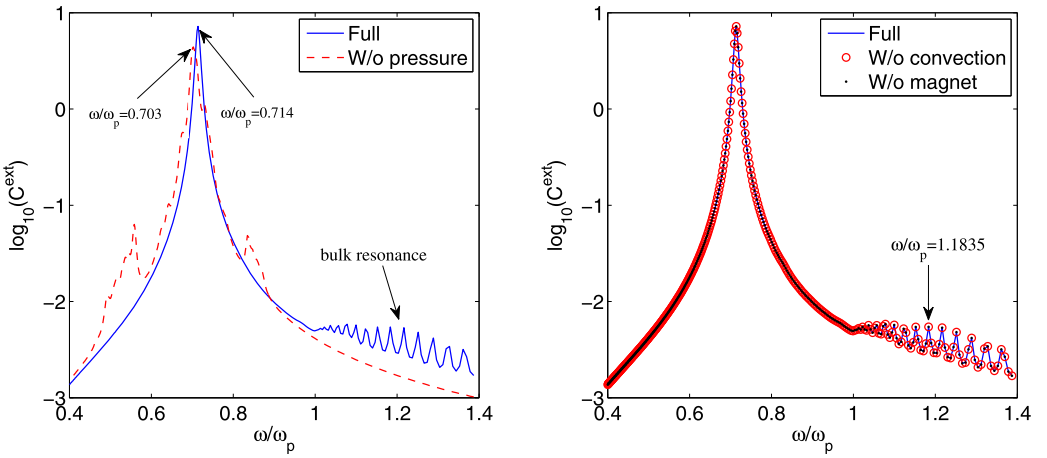

Fig. 12. ECS calculated by nonlinear HD model for Ag nanowire with radius $r = 2.0$.

Finally, we investigate the high order harmonic generation from a L-shaped metallic nanostructure, with a rectangular non-metallic material occupied nanostructure being located at its corner (see the right of Fig. 6), to study the influence of bound electrons on the generation of high order harmonic waves. The simulation setting is the same as the L-shaped case. In the simulations, we set $n_b = 58.0$, $\omega_b = \sqrt{n_b q_e^2/m_e}$, $\gamma_b = 0.8\gamma$. In Fig. 11 (Left), spectrums of the linear and nonlinear optical responses are presented, in comparison with spectrums obtained from the L-shaped metallic nanostructure in the previous test. It can be observed that the SHG is enhanced when the interaction between the bound electrons and the external electromagnetic waves has been taken into account.

4.3. Nonlocal effect

For small optical particles, especially for particles with size down to subwavelength, apart from the surface plasmon, the bulk plasmon could be excited as well. In this test, we solve the HEFMEs in TE mode to investigate the nonlocal effect for the Ag nanowire. As in [10], we choose the nanowire with radius $r = 2.0$, the plasma frequency $\omega_p = 2.885 \times 10^{-2}$, and the damping constant $\gamma = 0.01\omega_p$. PML boundary conditions are employed in both $x-$ and y-directions. To resolve the ECS in the time domain, we introduce the x-polarized incident wave propagating in y-direction by the TF/SF technique and collect the Fourier-transformed total field and scattered field on the TF/SF boundary. The ECS is calculated as follows

$$
\begin{aligned}
C_{sca}(\omega) &= \frac{\int_F \mathbf{n}\cdot\mathbf{S}_{sca}(\omega)dl}{|\mathbf{S}_{inc}(\omega)|}\,,\\
C_{abs}(\omega) &= -\frac{\int_F \mathbf{n}\cdot\mathbf{S}_{tot}(\omega)dl}{|\mathbf{S}_{inc}(\omega)|}\,,\\
C_{ext}(\omega) &= C_{sca}(\omega) + C_{abs}(\omega)\,,
\end{aligned}
$$

where $\mathbf{n}$ denotes the outward unit normal to the TF/SF boundary F, and $\mathbf{S}_\triangle$ denotes the time averaged Poynting vector

$$
\mathbf{S}_\triangle(\omega) = \frac{1}{2}\mathbf{E}_\triangle(\omega)\times\mathbf{H}^*_\triangle(\omega)\,. \tag{18}
$$

Since this additional on-the-fly Fourier transform requires a big amount of computation, currently we can only provide P^2 results on uniform grids $\Delta x = \Delta y = 0.04$ for this test. And due to the very small difference of two different numerical fluxes, we here use RKDG-UW-LF scheme. We try to recover the normalized ECS with frequency ranges in $0.4\omega_p$-$1.4\omega_p$ [10]. In the simulations, we adopt a short Gaussian pulse with $t_b = 2.998$, $\lambda_0 = 300$ carrying effective information in the range $0.4\omega_p$-$1.4\omega_p$ to perform a broad-band calculation. We simulate the optical interaction for a long time such that the scattered field decays adequately into a steady state and we set the final time $T = 5.996 \times 10^4$ for this purpose. In Fig. 12, we present the ECS being normalized with respect to the diameter of nanowire as a function of the normalized angular frequency ω/ω_p. It can be seen from Fig. 12 that the bulk plasmon resonances beyond the plasma frequency can be excited with the 2D HEFMEs. A slight blue-shift (from $\omega/\omega_p = 0.703$ to $\omega/\omega_p = 0.714$) of the surface plasmon resonance has been retrieved in the ECS as well. In order to make a further exploration on the source for the appearance of bulk plasmon resonances, we switch off the different nonlinear terms (quantum pressure term: $k\rho^{5/3}$, convection terms: $\rho u_i u_j, i, j = x, y, z$, magnetic terms: $u_i H_j - u_j - H_i, (i, j) = (x, y), (y, z), (z, x)$) in the equation (8), and make the calculation of the ECS, respectively. It can be observed from Fig. 12 that, apart from the ECS calculated from the 2D HEFMEs without the quantum pressure term, i.e., the 2D NHD model, all other ECSs are in perfect match with the calculated ECSs associated

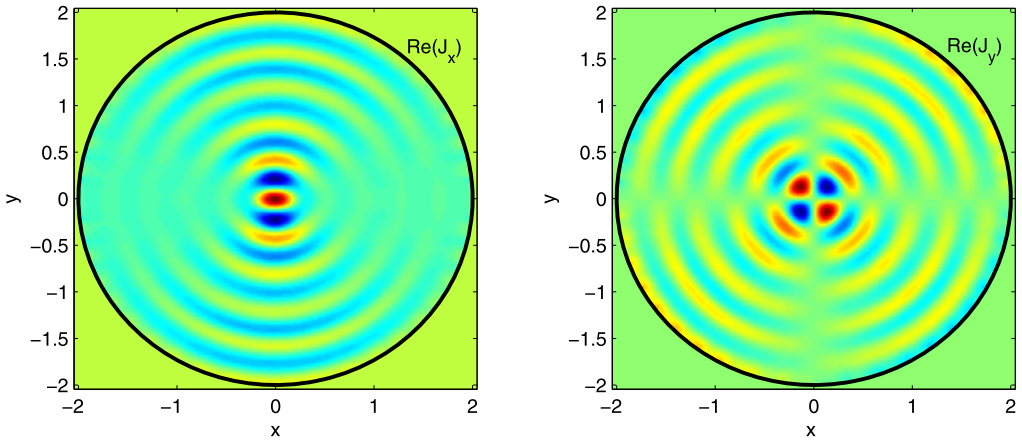

Fig. 13. The bulk plasmon resonances of the current density ($\omega/\omega_p = 1.1835$).

to the HEFMEs. This indicates that, among all three terms, the quantum pressure makes a unique contribution to appearance of the nonlocal effect. In Fig. 13, we provide with the Fourier-transformed current density at $\omega/\omega_p = 1.1835$. As it is shown, the resonances, namely the bulk plasmon, get excited in the bulk of nanowire.

5. Conclusions

In this paper, we develop an RKDG method for Maxwell's equations nonlinearly coupled with gas dynamic models with both the quantum pressure and bound electrons being taken into account. In particular, in addition to using Lax-Friedrichs numerical flux for electron fluid equation, we also consider using of the Harten-Lax-van-Leer numerical flux. It turns out that the proposed RKDG-UW-HLL scheme is more accurate than the RKDG-UW-LF scheme for HEFMEs. Numerical results show that high order harmonic waves can be produced from the L-shaped nanostructure and the rectangular nanostructure, and the bulk plasmon resonance can be excited for the metallic nanowire. The effect of bound electrons on the generation of high order harmonic waves has been confirmed in numerics. Meanwhile, a switch-on-and-off comparison reveals that the quantum pressure term in the HEFMEs is essentially important for the production of nonlocal effects. More advanced approximate Riemann solvers, numerical investigations on the influence of spill-out electrons on these important and complex optical phenomena associated to nanostructures with complex and irregular geometry, and three dimensional simulations will be envisioned in our future work.

Declaration of competing interest

The authors declare that they have no known competing financial interests or personal relationships that could have appeared to influence the work reported in this paper.

Acknowledgements

The work of M. Lyu is partially supported by the Chongqing University Graduate Student Research Innovation Project (Project No. CYS15018). The work of L. Jiang is partially supported by the Research Grants Council of Hong Kong GRF (Grant No. 17209918). The work of M. Li is partially supported by NSFC (Grant Nos. 11871139, 11701055). The work of L. Xu is partially supported by a Key Project of the Major Research Plan of NSFC (Grant No. 91630205) and a grant of NSFC (Grant No. 11771068).

References

[1] J.N. Anker, W.P. Hall, O. Lyandres, N.C. Shah, J. Zhao, R.P. Van Duyne, Biosensing with plasmonic nanosensors, Nat. Mater. 7 (2008) 442–453.
[2] V.A. Bokil, Y. Cheng, Y. Jiang, F. Li, Energy stable discontinuous Galerkin methods for Maxwell's equations in nonlinear optical media, J. Comput. Phys. 350 (2017) 420–452.
[3] S.I. Bozhevolnyi, V.S. Volkov, E. Devaux, J.-Y. Laluet, T.W. Ebbesen, Channel plasmon subwavelength waveguide components including interferometers and ring resonators, Nature 440 (2006) 508–511.
[4] X. Chen, O. Nadiarynkh, S. Plotnikov, P.J. Campagnola, Second harmonic generation microscopy for quantitative analysis of collagen fibrillar structure, Nat. Protoc. 7 (2012) 654–669.
[5] C. Ciraci, R.T. Hill, J.J. Mock, Y. Urzhumov, A.I. Fernandez-Dominquez, S.A. Maier, J.B. Pendry, A. Chilkoti, D.R. Smith, Probing the ultimate limits of plasmonic enhancement, Science 337 (2012) 1072–1074.
[6] B. Cockburn, C.-W. Shu, The Runge-Kutta discontinuous Galerkin method for conservation laws V: multidimensional systems, J. Comput. Phys. 141 (1998) 199–224.

[7] M. Fang, Z. Huang, W.E.I. Sha, X. Xiong, X. Wu, Full hydrodynamic model of nonlinear electromagnetic response in metallic metamaterials, Prog. Electromagn. Res. 157 (2016) 63–78.
[8] S. Gottlieb, C.-W. Shu, E. Tadmor, Strong stability preserving high order time discretization methods, SIAM Rev. 43 (2001) 89–112.
[9] A. Hille, M. Moeferdt, C. Wolff, C. Matyssek, R. Rodríguez-Oliveros, C. Prohm, J. Niegemann, S. Grafström, L.M. Eng, K. Busch, Second harmonic generation from metal nano-particle resonators: numerical analysis on the basis of the hydrodynamic Drude model, J. Phys. Chem. C 120 (2016) 1163–1169.
[10] K.R. Hiremath, L. Zschiedrich, F. Schmidt, Numerical solution of nonlocal hydrodynamic Drude model for arbitrary shaped nano-plasmonic structures using Nédélec finite elements, J. Comput. Phys. 231 (2012) 5890–5896.
[11] J.D. Jackson, Classical Electrodynamics, 3rd ed., Wiley, 1999.
[12] M.W. Klein, C. Enkrich, M. Wegener, S. Linden, Second-harmonic generation from magnetic metamaterials, Science 313 (2006) 502–504.
[13] M.W. Klein, M. Wegener, N. Feth, S. Linden, Experiments on second- and third-harmonic generation from magnetic metamaterials, Opt. Express 15 (2007) 5238–5247.
[14] A.V. Krasavin, P. Ginzburg, G.A. Wurtz, A.V. Zayats, Nonlocality-driven supercontinuum white light generation in plasmonic nanostructures, Nat. Commun. 7 (2016) 11497.
[15] S. Lal, S.E. Clare, N.J. Halas, Nanoshell-enabled photothermal cancer therapy: impending clinical impact, Acc. Chem. Res. 41 (2008) 1842–1851.
[16] J. Liu, M. Brio, Y. Zeng, A.R. Zakharian, W. Hoyer, S.W. Koch, J.V. Moloney, Generalization of the FDTD algorithm for simulations of hydrodynamic nonlinear Drude model, J. Comput. Phys. 229 (2010) 5921–5932.
[17] T. Lu, P. Zhang, W. Cai, Discontinuous Galerkin methods for dispersive and lossy Maxwell's equations and PML boundary conditions, J. Comput. Phys. 200 (2004) 549–580.
[18] M. Lyu, V.A. Bokil, Y. Cheng, F. Li, L. Xu, Energy stable discontinuous Galerkin method for nonlinear Maxwell's equations in mixed order form, Preprint.
[19] F.B.P. Niesler, N. Feth, S. Linden, J. Niegemann, J. Gieseler, K. Busch, M. Wegener, Second-harmonic generation from split-ring resonators on a GaAs substrate, Opt. Lett. 34 (2009) 1997–1999.
[20] R.G. Parr, W. Yang, Density-Functional Theory of Atoms and Molecules, Oxford Univ. Press, 1994.
[21] C.K.N. Patel, Efficient phase-matched harmonic generation in Tellurium with a CO_2 laser at 10.6μ, Phys. Rev. Lett. 15 (1965) 1027–1030.
[22] J. Qiu, B.C. Khoo, C.-W. Shu, A numerical study for the performance of the Runge-Kutta discontinuous Galerkin method based on different numerical fluxes, J. Comput. Phys. 212 (2006) 540–565.
[23] M. Scalora, M.A. Vincenti, D. de Ceglia, V. Roppo, M. Centini, N. Akozbek, M.J. Bloemer, M. Centini, Second and third harmonic generation in metal-based nanostructures, Phys. Rev. A 82 (4) (2010) 5929.
[24] N. Schmitt, C. Scheid, S. Lanteri, A. Moreau, J. Viquerat, A DGTD method for the numerical modeling of the interaction of light with nanometer scale metallic structures taking into account non-local dispersion effects, J. Comput. Phys. 316 (2016) 396–415.
[25] N. Schmitt, C. Scheid, J. Viquerat, S. Lanteri, Simulation of three-dimensional nanoscale light interaction with spatially dispersive metals using a high order curvilinear DGTD method, J. Comput. Phys. 373 (2018) 210–229.
[26] H. Sonnenberg, H. Heffner, Experimental study of optical second-harmonic generation in silver, J. Opt. Soc. Am. 58 (1968) 209–212.
[27] A. Taflove, Computational Electrodynamics: The Finite-Difference Time-Domain Method, Artech House, London, 1995.
[28] G. Toscano, J. Straubel, A. Kwiatkowski, C. Rockstuhl, F. Evers, H. Xu, N.A. Mortensen, M. Wubs, Resonance shifts and spill-out effects in self-consistent hydrodynamic nanoplasmonics, Nat. Commun. 6 (2015) 7312.
[29] F. Vidal-Codina, N.C. Nguyen, S.-H. Oh, J. Peraire, A hybridizable discontinuous Galerkin method for computing nonlocal electromagnetic effects in three-dimensional metallic nanostructures, J. Comput. Phys. 355 (2018) 548–565.
[30] L. Fraccarollo, E.F. Toro, Experimental and numerical assessment of the shallow water model for two-dimensional dam-break type problems, J. Hydraul. Res. 33 (1995) 843–864.
[31] P. Wasylczyk, I.A. Walmsley, W. Wasilewski, C. Radzewicz, Broadband noncollinear optical parametric amplifier using a single crystal, Opt. Lett. 30 (2005) 1704–1706.
[32] Y. Zeng, W. Hoyer, J. Liu, S.W. Koch, J.V. Moloney, A classical theory for second-harmonic generation from metallic nanoparticles, Phys. Rev. B 79 (2009) 235109.
[33] Y. Zhao, J. Liu, FDTD for hydrodynamic electron fluid Maxwell equations, Photonics 2 (2015) 459–467.